FISEVIER

Contents lists available at ScienceDirect

Thin-Walled Structures

journal homepage: www.elsevier.com/locate/tws



Full length article

Size-dependence of AM Ti–6Al–4V: Experimental characterization and applications in thin-walled structures simulations



Junyan He ^a, Shashank Kushwaha ^{a,1}, Mahmoud A. Mahrous ^{b,1}, Diab Abueidda ^c, Eric Faierson ^d, Iwona Jasiuk ^{a,*}

- a Department of Mechanical Science and Engineering, University of Illinois at Urbana-Champaign, Champaign, IL, USA
- b Department of Civil and Environmental Engineering, University of Illinois at Urbana-Champaign, Champaign, IL, USA
- c National Center for Supercomputing Applications, University of Illinois at Urbana-Champaign, Champaign, IL, USA
- d Department of Materials Science and Engineering, Iowa State University, Ames, IA, USA

ARTICLE INFO

Keywords: Size effects Selective laser melting Ti-6Al-4V Specific energy absorption Thin-walled lattice structures Topology optimization

ABSTRACT

Previous studies show that the properties of parts manufactured via additive manufacturing, such as selective laser melting, depend on local feature sizes like lattice wall thickness and strut diameter. Although size dependence has been studied extensively, it was not included in constitutive models for numerical simulations. In this work, flat dog-bone tensile specimens of different thicknesses were manufactured and tested under quasi-static conditions to characterize the size-dependent properties experimentally. It was observed that key mechanical properties decrease with specimen thickness. Through curve-fitting to experimental data, this work provides approximate analytical expressions for the material properties values as a function of specimen thickness, furnishing a phenomenological size-dependent constitutive model. The interpolating capability of the model is cross-validated with existing experimental data. Two numerical examples demonstrate the application of the size-dependent material model. The axial crushing of thin-walled lattices at varying wall thicknesses was simulated by the size-dependent material model and one that ignores size effects. Results show that ignoring size effects leads to overestimated peak crushing force and specific energy absorption. The two material models were also compared in the topology optimization of thin-walled structures. Results show that the size-dependent model leads to a more robust optimized design: having higher energy absorption and sustaining less material fracture.

1. Introduction

Advances in metal additive manufacturing (AM) techniques have allowed them to grow from a prototyping technology into industrial production [1,2]. A commonly used metal AM technique is selective laser melting (SLM), where a laser traces the cross-section of the part and melts the deposited metal powder along its path. The part is printed in a layer-by-layer fashion, where a new layer of metal powder is deposited once the laser finishes tracing the current layer. AM removes many constraints and limitations imposed by traditional subtractive manufacturing methods, thus allowing parts with complicated geometries to be built. Many previous studies have manufactured lattice structures using AM, such as thin-walled lattice structures like honeycombs [3–5], gyroids [6,7], and various truss-based lattices [8,9].

The mechanical properties of the manufactured lattice structures depend on AM process parameters such as laser scan speed [10], scan strategy [11], build direction [12], and the part surface finish [13]. When performing finite element (FE) simulations for AM

parts, the effects of these process parameters are typically taken into account by calibrating the material model using tensile specimens manufactured by the same AM process parameters [14,15]. However, the standard tensile specimens may not share similar characteristic dimensions (such as wall thickness and strut diameter) as the AM parts, which is especially true for thin-walled and truss-based lattices, where the manufactured lattices may have wall thickness or strut diameter much smaller than typical tensile test specimens. Previous studies have shown that the mechanical properties of SLM parts depend on the local feature size [16-20]. In general, it was found that crucial mechanical properties, such as Young's modulus, yield stress, ultimate tensile stress, and elongation to failure, decrease as the wall thickness or strut diameter decreases. The reduction in elastic properties with decreasing thickness can be attributed to the increase in porosity levels of the part [17,20] and the decrease in the actual load-bearing area due to specimen surface roughness caused by geometric inaccuracy of the manufacturing process [18]. The reduction in yield stress, ultimate

^{*} Corresponding author.

E-mail address: ijasiuk@illinois.edu (I. Jasiuk).

¹ Both authors contributed equally to this work.

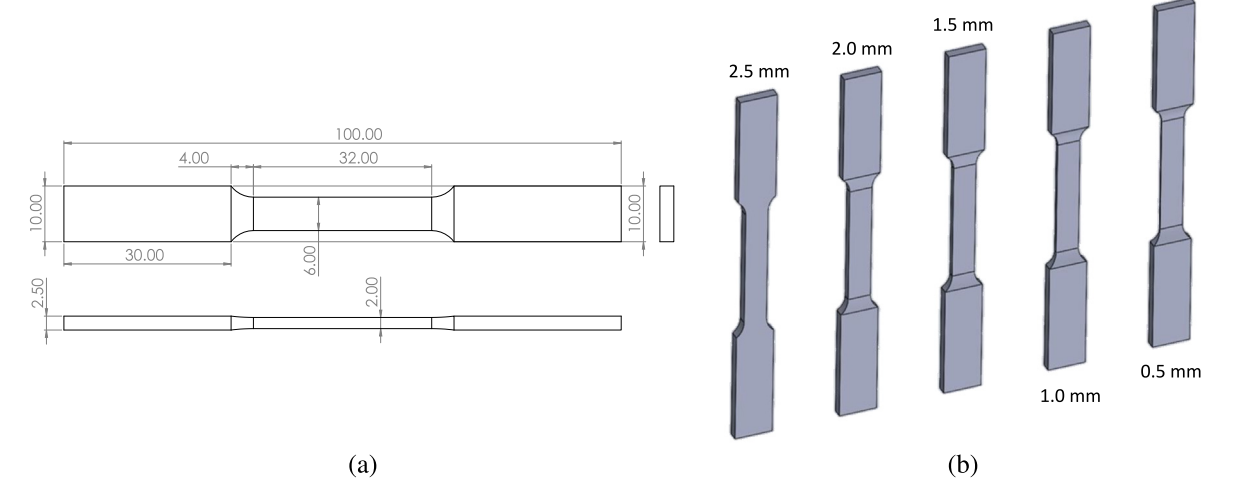


Fig. 1. Tensile specimens: (a) Technical drawing showing the specimen dimensions in mm. (b) CAD rendering of specimens with different thicknesses.

strength, and failure strain can be attributed to the stress concentration effects of the surface roughness. As the specimen thickness (or other characteristic dimensions) decreases, the depth (or amplitude) of the surface roughness accounts for a more significant portion of its cross-sectional area. Thus, the mechanical properties degrade when specimen size is small [16,18]. Other physical evidence for these size-dependent material properties includes the changing oxygen content [16] and the change in microstructures induced by the manufacturing process and part geometry [16,18,20]. It is also important to note that the size effects discussed in this work are mainly due to the manufacturing processes and are different from the size effects described by strain-gradient plasticity theories [21–23]. Those are caused by the non-negligible contribution of geometrically necessary dislocations and occur at a length scale much smaller than the characteristic thickness (about 1 mm) discussed in this work.

To capture the effects of surface roughness and the apparent sizedependent macroscopic properties, researchers have attempted to resolve the surface roughness and internal voids explicitly in the FE models [18,19,24]. When surface roughness is explicitly modeled, the FE simulations can predict the size-dependent ultimate strength [18] and provide a much better prediction of buckling load than an idealized CAD design geometry of the truss-based lattice [19,24]. However, resolving these small-scale features on the mesh requires solid continuum elements, which are computationally expensive and limit their applications in specimen-scale simulations. For larger, component-scale simulations of lattices, shell elements are typically used for thin-walled lattices, and beam elements are commonly used for truss-based lattices. These simplified FE geometric representations cannot resolve smallscale details like surface roughness and void. Thus, a homogenized, size-dependent material model is needed to capture the thicknessdependent mechanical properties in a phenomenological manner.

This work has two main objectives. First, to characterize the thickness dependence of key mechanical properties on SLM specimens. Second, curve fitting to experimental data to produce approximate analytical expressions that describe the thickness-dependence of material model parameters, thus leading to a phenomenological, size-dependent constitutive model.

The strong influence of specimen thickness on yield stress and ultimate strength indicates that properties measured on thicker/larger tensile specimens may not be representative of those in the AM-printed thin-walled lattices, which typically have a much smaller wall thickness. Therefore, using properties measured from larger specimens may overestimate lattice performance metrics like specific energy absorption (SEA) and peak crushing force (PCF). In addition, ignoring size effects in topology optimization (TO) of thin-walled lattices may lead

Table 1
SLM process parameters used for manufacturing the tensile specimens.

Process parameter	Hatch parameters	Border parameters		
Distance between borders [mm]	/	0.11		
Number of borders	/	2		
Laser power [W]	400	225		
Point distance [µm]	80	20		
Hatch distance [mm]	0.1	/		
Laser scan speed [mm/s]	1142.9	500		
Layer height [mm]	0.06	0.06		
Scan pattern	Stripe	/		

to less robust designs. We demonstrate these two points through two numerical examples.

This paper is organized as follows: Section 2 provides detail on the specimen fabrication, experimental setup, and constitutive modeling. Section 3 presents and discusses the experimental results and the two numerical examples. Section 4 summarizes the outcomes, limitations, and highlights possible future works.

2. Materials and methods

2.1. Specimen fabrication

The material considered in this work is Ti–6Al–4V Grade 23, with raw metal powder sourced from AP&C Powder Metallurgy. The powder has an oxygen content of 0.11% and the powder diameters range from 15 to 45 μm . SLM technology was used to manufacture the specimens, with a Renishaw machine located in the Quad City Manufacturing Laboratory. The SLM process parameters used to manufacture the specimens were default Renishaw build settings for Ti–6Al–4V. Since the objective of this work is not to study the effects of process parameters on the properties of the specimens, we did not modify these parameters during the manufacturing process. The selected parameters are listed in Table 1.

A technical drawing of the tensile specimens and the CAD rendering are shown in Fig. 1. The dimensions of the specimens largely follow ASTM E8/E8M-13a standard for subsize specimens. Slight modifications were made so that all grip sections have a constant thickness of 2.5 mm regardless of the gauge region thickness (ASTM E8 standard uses a single thickness throughout the specimen) for easier gripping and to avoid failure at the grips. Fillets were added to smoothly transition between the grip thickness and the thickness of the gauge region. This geometry modification is assumed to have a negligible effect on the testing results. All specimens share a common length of the reduced



Fig. 2. Experimental setup for the tensile tests.

section at 32 mm and a width of 6 mm. Five specimen thicknesses were considered. They were 0.5, 1.0, 1.5, 2.0, and 2.5 mm. For each thickness, six specimens were manufactured. All specimens were built vertically with no support material, a typical way to manufacture thin-walled lattices with a constant in-plane cross-section. Previous experimental studies show that build direction affects the mechanical properties of the parts [19,25,26]. This effect is not examined in this work, and we maintained a single upright build direction for all specimens. All specimens were stress relieved at 650 °C for 3 h in argon gas.

2.2. Tensile tests

All samples were tested at room temperature using an Instron 1332 servo-hydraulic testing machine (Instron, MA, USA) with a crosshead speed of 0.1 mm/s. A 50 kN load cell was used to measure the load at a sampling rate of 50 Hz. An IEEE 1394 digital camera from IMI TECH was used to take images of the specimens during the test at a frame rate of 3.75 Hz for 2D digital image correlation (DIC) analysis. Since no polishing was applied to the specimen surfaces, the as-printed surface roughness provided sufficient contrast under the polarizing lens, and thus no additional speckle pattern was applied to the specimen surfaces. The camera was positioned to face the width of the specimens. The processing of the DIC images and strain calculation were completed in VIC-2D (Correlated Solutions, Columbia, SC, USA). The complete experimental setup is shown in Fig. 2. The Young's modulus, yield stress, and elongation to failure were extracted from the experiment data.

2.3. Constitutive model

Besides experimental characterization, this work also proposes a size-dependent material model suitable for FE simulations. For simplicity, the material was assumed to be isotropic, whose elastic response is characterized by a thickness-dependent Young's modulus E(t) (thickness is denoted by t) and a constant Poisson's ratio of 0.31 [27].

We adopted the modified Voce hardening model [28] for the plastic behavior of Ti–6Al–4V. The yield stress is given by:

$$\sigma_y(\bar{\epsilon}^p) = Y_0 + R_0\bar{\epsilon}^p + R_{inf} \left(1 - \exp(-b\bar{\epsilon}^p) \right). \tag{1}$$

where \bar{e}^p , Y_0 , R_0 R_{inf} , and b denote the equivalent plastic strain and thickness-dependent material parameters to be determined through curve fitting to experimental data, respectively. The damage and fracture behavior of Ti–6Al–4V is modeled by the element deletion technique [29], which necessitates the definition of a critical value of equivalent plastic strain at the onset of material damage and fracture energy. The equivalent plastic strain at the onset of damage, \bar{e}^p_{ini} , is a thickness-dependent material parameter to be determined iteratively by matching the FE-predicted elongation to failure with that observed by experiments. Material damage is said to occur in FE simulations when $\bar{e}^p \geq \bar{e}^p_{ini}$. Beyond damage initiation, the stress tensor is reduced by a damage variable D as [29]:

$$\sigma = (1 - D)\sigma_0,\tag{2}$$

where σ_0 is the stress computed from the unmodified material properties; fracture occurs when D=1. The evolution law for D is given by [29]:

$$\dot{D} = \frac{\sigma_y L}{2G_f} \dot{e}^p, \tag{3}$$

where L, G_f , and $\dot{\varepsilon}^p$ denote the characteristic length of the finite element, fracture energy per unit area, and equivalent plastic strain rate, respectively. The characteristic length of the finite element is used in the damage evolution to minimize mesh dependence of the solution following the proposal of Hillerborg [29,30].

Besides the equivalent plastic strain at the onset of material damage, the fracture energy G_f is another key parameter in the damage model. Just like other material parameters considered in this work, it is reasonable to assume that G_f is thickness dependent. However, the camera frame rate used in this work (3.75 Hz) did not provide sufficient temporal resolution to resolve the rapid fracture process during the experiment, so it was difficult to obtain accurate measurements of the fracture process to characterize the damage evolution behavior. An inspection of the fractured specimens shows a negligible amount of necking, and as seen in Section 3.1, the specimen failure behavior is abrupt, with negligible softening before failure. Therefore, in the lack of available experimental data, we assumed constant fracture energy and only focused on the size dependence of damage initiation strain as a first approximation. The value of the fracture energy follows from the work of Wang et al. [27], which is an experimentally validated material parameter set for machined Ti-6Al-4V.

To summarize, a thickness-dependent constitutive model for Ti-6Al-4V can be fully characterized by Young's modulus E, parameters in the modified Voce hardening model Y_0 , R_0 , R_{inf} , and b, as well as damage parameter $\bar{\epsilon}^p_{ini}$. In the next section, we provide analytical expressions that relate these material parameters to the specimen thickness t.

3. Results and discussion

In this section, we present the experimental results and the fitted equations for the material model parameters. After comparing the FE-simulated response with the uniaxial tensile experiments, we show two numerical examples to demonstrate how a size-dependent material model affects: (1) performance prediction of thin-walled lattice structures with varying wall thickness and (2) topology optimization (TO) of thin-walled lattice structures. All FE simulations were conducted using 10 high-end AMD EPYC 7763 Milan CPU cores on Delta, an HPC cluster hosted at the National Center for Supercomputing Applications (NCSA).

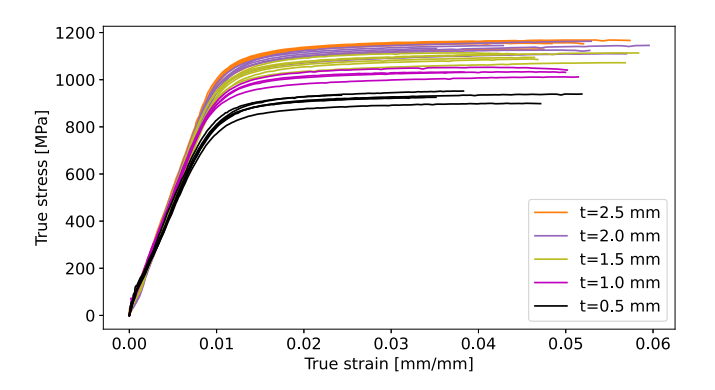


Fig. 3. Stress-strain curves for SLM Ti-6Al-4V at different specimen thickness. (For interpretation of the references to color in this figure legend, the reader is referred to the web version of this article.)

3.1. Experiment results and fitted elastic and plastic material parameters

The experimentally measured load (from load cell) and strain (from digital image correlation) results were converted to true stress–strain curves for different specimen thicknesses and are shown in Fig. 3. The Young's modulus, 0.2% offset yield stress, and elongation to failure were extracted from the stress–strain curves and summarized in the bar charts in Fig. 4.

All experimentally obtained data points from specimen thicknesses 2.5, 2, 1, and 0.5 mm were used in the curve fitting to obtain the material parameters. The data from the 1.5 mm specimen thickness were not used in the curve fitting process and were instead saved as cross-validation for the fitted analytical expressions. We seek an analytical dependence on specimen thickness in the range $t \in [0.5, 2.5]$ mm for all material parameters. The nonlinear least square fitting function *curve fit* from the Scipy [31] optimization package was used to perform curve fitting. To measure the quality of the curve fit for a parameter a, we calculate the mean relative difference (MRD), defined as:

$$MRD_{a} = \frac{\sum_{i}^{N} |a_{i}^{exp} - a_{i}^{fit}|}{\sum_{i}^{N} a_{i}^{exp}} \times 100\%. \tag{4}$$

where i is the index of the experimental data point, and N is the total number of available data points.

Young's modulus was fitted to an exponential-type equation of the form:

$$y = a_0 (1 - \exp(-a_1 t)) + a_2.$$
 (5)

Here, an exponential-type curve-fitting equation is used instead of a polynomial form since it is reasonable to assume the existence of a critical thickness value, beyond which size effects are negligible, and the material properties approach a plateau value. This assumption is supported by our experimental measurements in Fig. 4 and previous literature findings [17,18]. The experimentally measured Young's modulus for each thickness is shown in Fig. 5 as box-and-whisker plots along with the fitted curve. The analytical functional dependence is given by:

$$E(t) = 45979.1 [1 - \exp(-2.2t)] + 55918.2$$
 [MPa]. (6)

The fitted expression agrees well with the mean values of the four thicknesses used in the curve fitting, although slightly over-predicting the mean Young's modulus for the validation set (1.5 mm thickness). Nonetheless, we note that the fitted curve is within the observed specimen-to-specimen variation, and the MRD is 2.6%, which indicates a satisfactory fit.

A two-stage fitting process is required for the four material parameters in the modified Voce hardening model. First, the four parameters for each stress-strain curve must be determined, which is done by

fitting the portion of the stress–strain curve above the elastic limit (defined by $\epsilon_p > 4 \times 10^{-4}$ ²) to Eq. (1). Once we obtained the parameters for each stress–strain curve, we performed curve fitting for each parameter to obtain the size dependence, again reserving the 1.5 mm thickness data from cross-validation. For parameters Y_0 and R_{inf} , the exponential function of the form in Eq. (5) was used. The box-and-whisker plots and the fitted curves are shown in Fig. 6. The analytical functional dependencies for Y_0 and R_{inf} are given by:

$$Y_0(t) = 432.6 [1 - \exp(-0.4t)] + 686.0 \text{ [MPa]},$$

 $R_{inf}(t) = 274.1 [1 - \exp(-4.8t)] - 126.2 \text{ [MPa]}.$ (7)

The fitted expressions show a decent fit with experimental data, falling within the specimen-to-specimen variation of the validation data points. The MRDs are 2.3% and 8.8% for Y_0 and R_{inf} , respectively.

The parameter R_0 , due to its oscillatory data distribution and lack of a consistent trend, is considered size-independent, and the mean value over all the curve-fitting data points was used as the fitted value, which was found to be 1298.7 MPa. A comparison of this mean value with the box-and-whisker plots of the raw data is shown in Fig. 7(a), and using a constant value results in an MRD of 21.4%. For the parameter b, a slightly different exponential form was used in the curve fitting; it is given by:

$$y = a_0 \left(1 - \exp(-a_1(t - a_2)) \right) + a_3. \tag{8}$$

The fitted curve and box-and-whisker plots are compared in Fig. 7(b). The analytical functional dependence is given by:

$$b(t) = 23.1 \left[1 - \exp(-1.5(t - 2.0))\right] + 364.5. \tag{9}$$

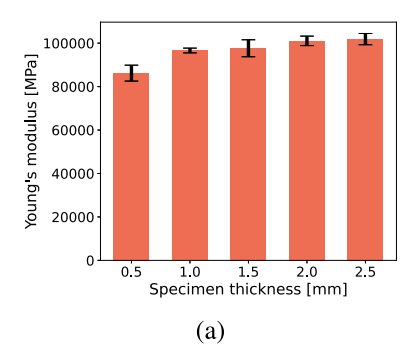
This curve fit leads to a satisfactory fit with an MRD of 7.9%, and the fitted curve agrees well with the mean value of the validation data.

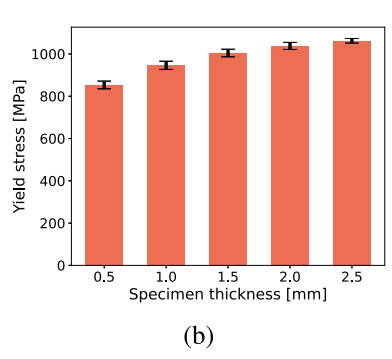
The approximate analytical expressions in (6), (7) and (9) provide the dependence of the elastic and plastic material parameters on the specimen thickness.

3.2. Mesh convergence study and damage model parameter

The equivalent plastic strain at damage initiation $\bar{\epsilon}^p_{ini}$ is needed in the definition of the damage model, which is different from the experimentally measured elongation to failure. The former is a local measure, while the latter is a global, average measure of failure. Therefore, as mentioned in Section 2.3, $\bar{\epsilon}^p_{ini}$ was obtained by iteratively fitting the FE simulations to the experimentally measured elongation to failure. The FE simulation was conducted in Abaqus/Explicit [29] using C3D8R finite elements. An explicit dynamic simulation was used for easier convergence with the damage model. For simplicity, only the rectangular gauge region for each specimen was modeled. Before using this model to calibrate the damage model, a mesh convergence study was conducted. Three meshes were generated with 5, 6, and 7 elements through the specimen thickness. A constant aspect ratio of 2 was used to determine the in-plane mesh size based on the corresponding element thickness to maintain good-quality elements. The size-dependent elastic and plastic properties defined in Section 3.1 and a constant \bar{e}_{ini}^p of 0.05 were used to test mesh independence of the failure behavior. 6% strain was applied under displacement control over 1 s, and the simulation was conducted under a time increment of 5×10^{-6} s. The displacements and reaction forces were extracted from the simulation and converted to the simulated stress-strain curves. The FE mesh, boundary conditions, and simulated responses are depicted in Fig. 8. Based on the results shown in Fig. 8(b), a mesh with 5 elements through thickness was sufficient to achieve convergence with the elastic-plastic and damage response. This mesh was used in subsequent damage material model calibration.

 $^{^2}$ $\epsilon_p = \epsilon_{total} - \frac{\sigma}{E}$ is the axial plastic strain, and a threshold of 4×10^{-4} instead of 0 was used to exclude small initial noise in experimental data.





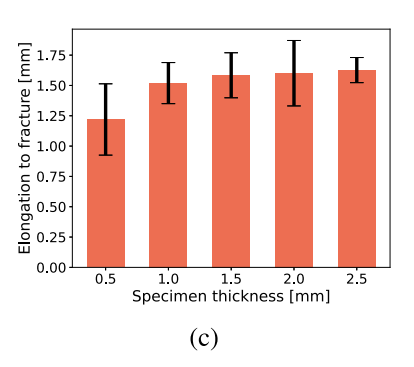


Fig. 4. Experimentally measured mechanical properties: (a) Young's modulus. (b) 0.2% offset yield stress. (c) Elongation to fracture. The error bars in the plots indicate the standard deviation across all samples.

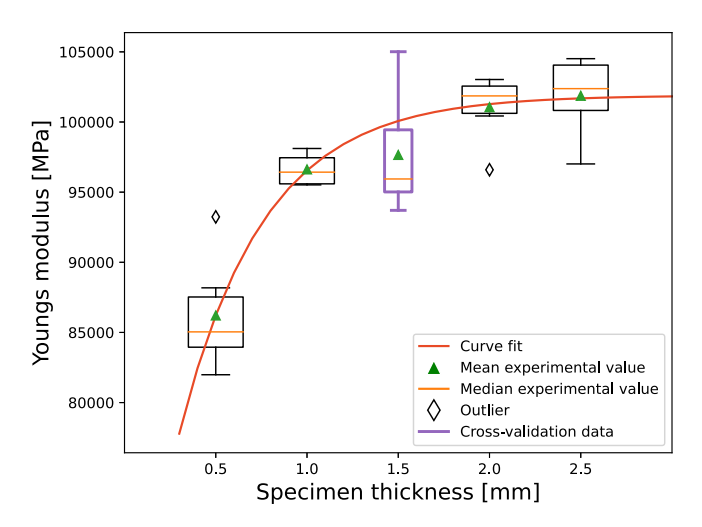


Fig. 5. The fitted thickness-dependent Young's modulus of Ti-6Al-4V compared to experimental observations. Cross-validation data (not used in curve fitting) is shown in purple. (For interpretation of the references to color in this figure legend, the reader is referred to the web version of this article.)

Table 2 FE-identified values of \bar{e}_{ini}^p at different thicknesses.

Specimen thickness [mm]	0.5	1.0	1.5	2.0	2.5
$ar{\epsilon}_{ini}^p$ [mm/mm]	0.0302	0.0428	0.0432	0.0480	0.0529

Due to the sensitivity of the damage behavior on the parameter $\bar{\epsilon}_{ini}^p$ and the large scattering observed in the experimentally measured elongation to failure, we focused on capturing the mean behavior of the size-dependent failure. Therefore, the mean elongation to failure was calculated for all thicknesses, and FE simulations were performed to determine the corresponding value of $\bar{\epsilon}_{ini}^p$ that best agrees with the mean elongation to failure behavior. The FE-identified values for $\bar{\epsilon}_{ini}^p$ are shown in Table 2.

The data points, except at 1.5 mm thickness, were used in fitting a model of the form given in Eq. (5) to obtain an approximate analytical relationship. The fitted curve is compared to all FE-identified \bar{e}_{ini}^{p} values in Fig. 9(a). The curve fit equation is shown in Eq. (10). The fitted curve yields a satisfactory representation of the FE-identified \bar{e}_{ini}^{p} values with an MRD of 4.2%, except slightly over-predicting at the cross-validation data.

$$\bar{e}_{ini}^p(t) = 0.0572 \left[1 - \exp(-1.0352t)\right] - 6.1621 \times 10^{-3} \text{ [mm/mm]}.$$
 (10)

FE simulations were conducted at all five thicknesses with the fitted $\bar{\epsilon}^p_{ini}$ values to evaluate the effect of the curve-fitting on the simulated elongation to failure. A comparison between the simulated elongation to failure and the box-and-whisker plots of the experimental data is shown in Fig. 9(b). From the comparison, we see that the curve-fitted $\bar{\epsilon}^p_{ini}$ values yield a satisfactory agreement with the mean elongation to

failure observed in the experiments. To show the agreement between experimental data and the curve-fitted material model over the entire stress–strain curve, we illustrate the FE-predicted response and the experimental measurements in Fig. 10.

The comparison shows that the fitted size-dependent material model well captures the mean response of the specimens over the entire range of the stress–strain curve, and the FE-predicted response falls within the specimen-to-specimen variations observed in the experiments. This result validates the proposed curve-fitting approach and the phenomenological size-dependent material model.

To summarize, the thickness-dependent material properties in Eqs. (6)–(10) furnish a size-dependent material model for SLM Ti–6Al–4V that covers the material's elastic, plastic, and damage behaviors. The thickness-dependent material model parameters were entered into Abaqus via data tables. A field variable T was introduced in the tables to represent specimen thickness, and the values of the material parameters at different field variable values (i.e., specimen thicknesses) were stored. A preprocessing step to assign field variable value to the FE model is needed to use this size-dependent material model on thinwalled structures. In this step, each element in the mesh is assigned a value of T based on its thickness. This value of T affects the element's constitutive behavior based on the size-dependent material model.

3.3. Material size effects and performance prediction of thin-walled lattices

A typical thin-walled lattice is the extruded lattice, which has a constant cross-section along its height. The in-plane geometry design can significantly affect the PCF and SEA of the lattices [32]. The PCF is defined as the maximum crushing force observed during loading, while the volume-based SEA of a lattice design is defined as:

$$SEA = \frac{1}{V} \int_0^{u_f} F \, du,\tag{11}$$

where V, F, u, and u_f denote the volume of the thin-walled lattice, reaction force, axial displacement, and final axial displacement, respectively. The authors [33] previously proposed a combinatorial framework to generate lattice cross-sections by randomly combining geometric features. The Johnson-Cook constitutive law was used to model the strain-rate-dependent material properties of Ti–6Al–4V under high strain rates. Still, the size effects were ignored when varying the wall thickness of the thin-walled lattice structures. In this example, we leverage the size-dependent material model in Section 3.1 to study how the inclusion of size effects influences the predicted PCF and SEA at different lattice wall thicknesses.

A lattice cross-section was randomly generated using the combinatorial framework detailed in [33], which has four unit cells, forming a 2×2 periodic arrangement. The in-plane cross section has a nominal dimension of 150×150 mm², with a height of 75 mm. The lattice structures were discretized using shell elements with constant shell thickness. Five thicknesses mentioned in Section 2.1 were considered. The lattice was compressed to 5% axial strain by a rigid plate with

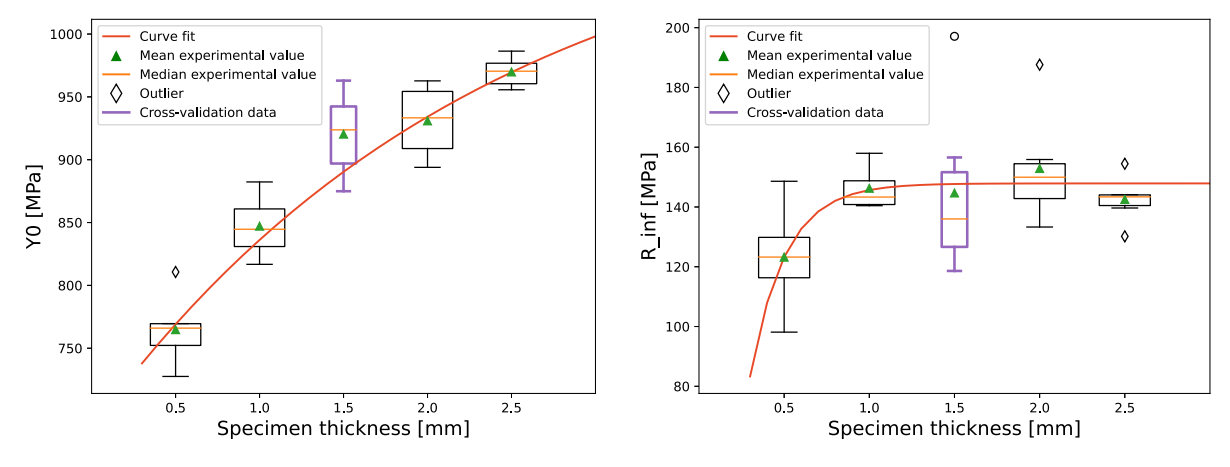


Fig. 6. The fitted thickness-dependent Y_0 and R_{inf} curves compared to individual values. Cross-validation data (not used in curve fitting) is shown in purple. (For interpretation of the references to color in this figure legend, the reader is referred to the web version of this article.)

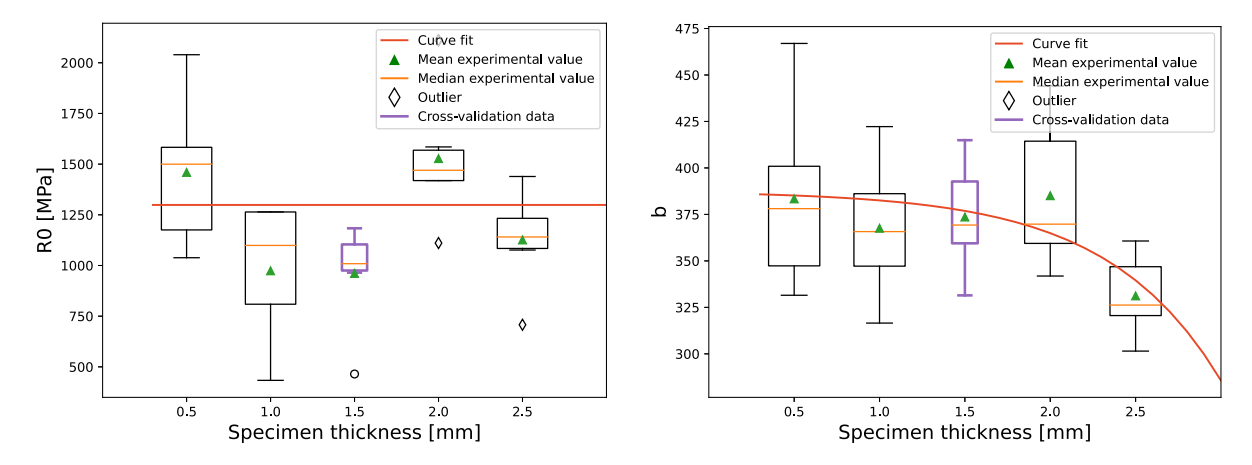


Fig. 7. The fitted thickness-dependent R_0 and b curves compared to individual values. Cross-validation data (not used in curve fitting) is shown in purple. (For interpretation of the references to color in this figure legend, the reader is referred to the web version of this article.)

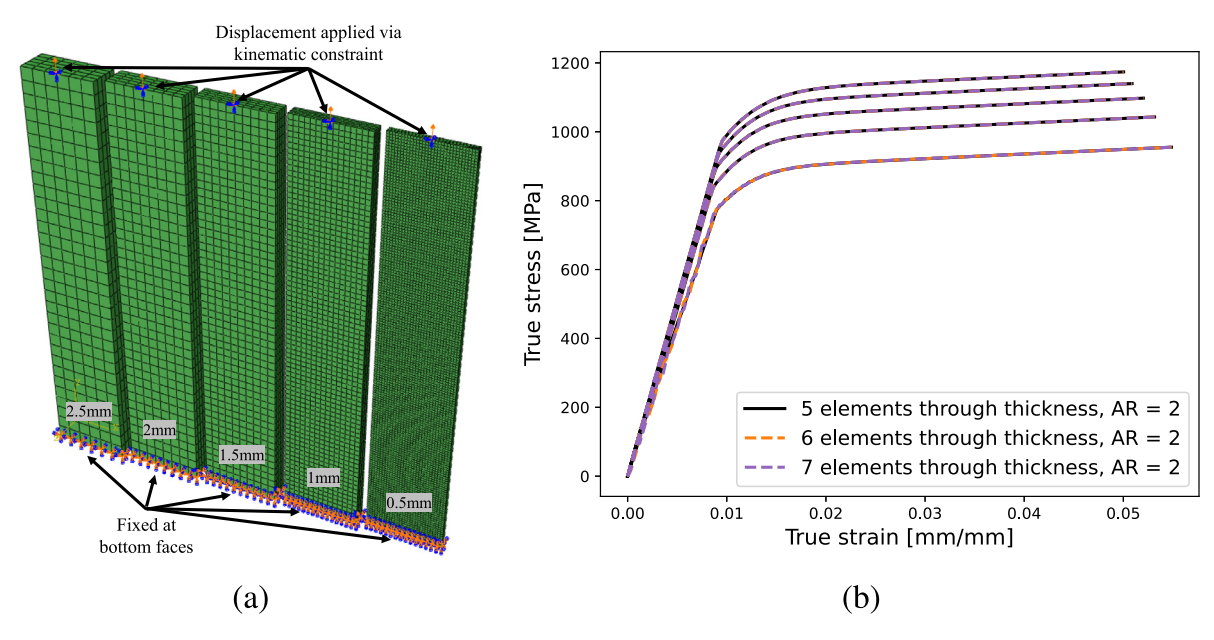


Fig. 8. Mesh convergence study for parameter calibration: (a) Mesh and applied boundary conditions. (b) Simulated responses from three meshes.

a constant velocity of 250 mm/s. Since the material model was calibrated at quasi-static loading conditions, the effects of strain rate on the material constitutive response were ignored. General contact in

Abaqus/Explicit was used for contact between parts and self-contact with hard behavior in the normal direction and frictionless behavior in the tangential direction. Two material models were considered: (1)

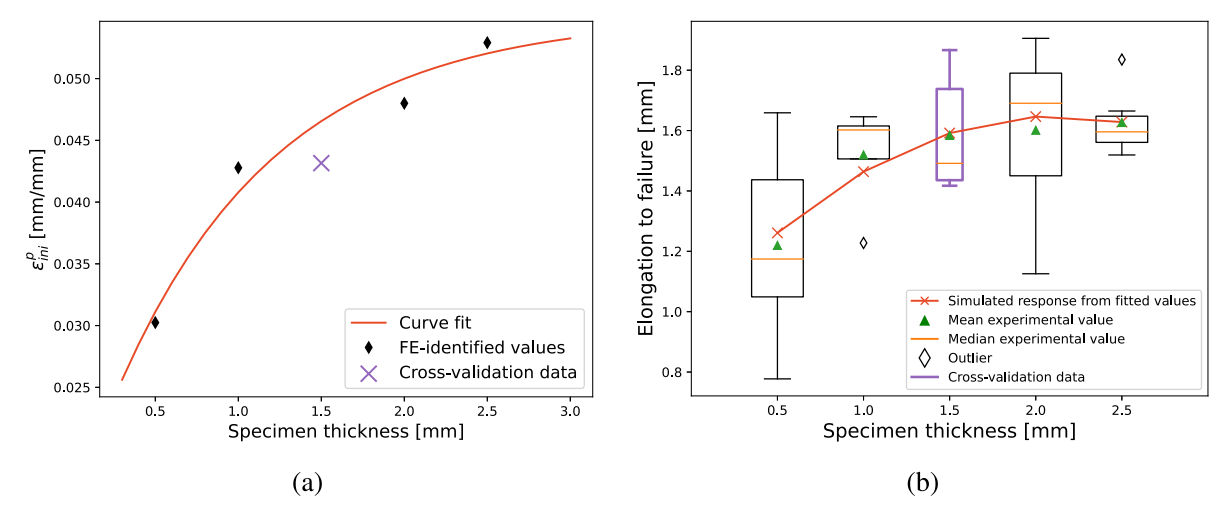


Fig. 9. Calibration of the damage model: (a) The fitted thickness-dependent damage initiation strains compared to individual FE-identified values. (b) Comparison of simulated and experimentally observed elongation to failure. (For interpretation of the references to color in this figure legend, the reader is referred to the web version of this article.)

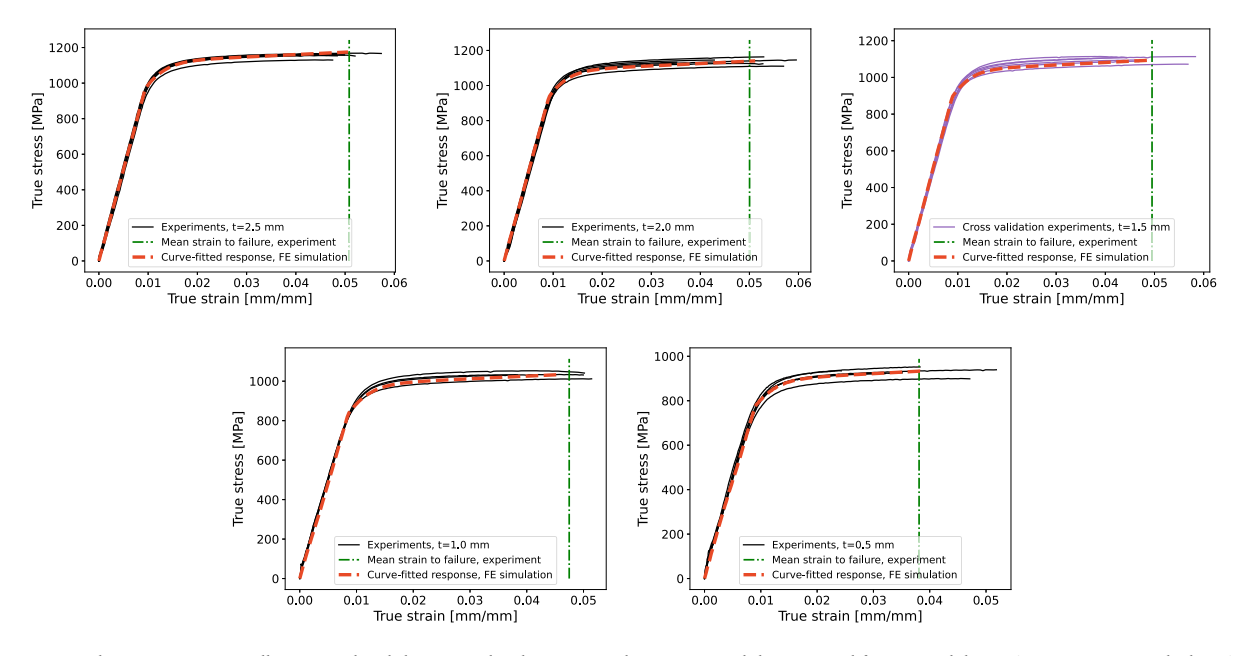


Fig. 10. Comparison between experimentally measured and the FE-simulated responses. The experimental data reserved for cross-validation (1.5 mm specimen thickness) is marked with purple and was not used in curve fitting. The mean strain to failure observed in the experiments is indicated in green. (For interpretation of the references to color in this figure legend, the reader is referred to the web version of this article.)

size-dependent model (subsequently denoted as SDM) in Section 3.1. (2) constant model (subsequently denoted as CM), where all properties were taken from the 2.5 mm specimen data irrespective of the wall thickness. 2.5 mm was chosen since typical tensile specimen thicknesses are larger than the wall thickness of the thin-walled lattices. The force-displacement curve was recorded, and SEA was calculated from it.

Mesh convergence was studied on three meshes with 38 880, 75 600, and 154 080 linear shell elements with reduced integration (S4R). SDM was used for the constitutive model, and the shell thickness was 1.5 mm. The FE mesh, boundary conditions, and simulated responses are depicted in Fig. 11. Based on the results shown in Fig. 11(b), the mesh with 75 600 elements (uniform mesh size of 1 mm) was sufficient to achieve force—displacement curve convergence, which was used in this example.

The lattice cross section and the simulated PCFs and SEAs are shown in Fig. 12. We define the percent difference (PD) in predicted values between two material models for a metric X as:

Table 3
Percent difference in performance metrics predicted by two material models.

Specimen thickness [mm]	2.5	2.0	1.5	1.0	0.5	Mean
PD _{PCF} [%]	0.0	2.8	6.7	12.7	19.2	8.3
PD_{SEA} [%]	0.0	3.0	7.0	20.4	37.6	13.6

$$PD_X = \frac{X_{CM} - X_{SDM}}{X_{SDM}} \times 100\%,$$
 (12)

where subscript $_{SDM}$ denotes the size-dependent material model, and $_{CM}$ denotes the constant material model. A positive percent difference means that the constant material model overestimates the metric X. The percent differences for PCF and SEA are reported in Table 3.

The force-displacement curves for the 0.5 mm-thick lattice predicted by both material models are compared in Fig. 13. For further discussion, four critical strain points have been marked in Fig. 13. They are: (1) immediately after peak load, 0.99% strain; (2) during first major fracture, 1.05% strain; (3) end of first major fracture, 1.2%; and (4) end of compression, 5% strain.

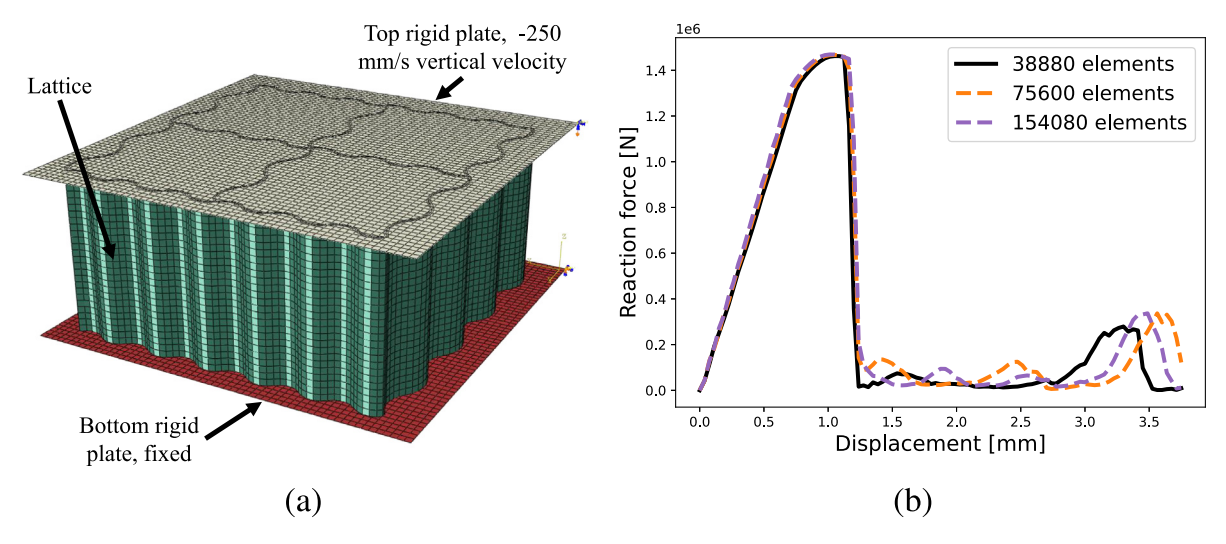


Fig. 11. Mesh convergence study for axial compression: (a) Mesh and applied boundary conditions. (b) Simulated responses from three meshes.

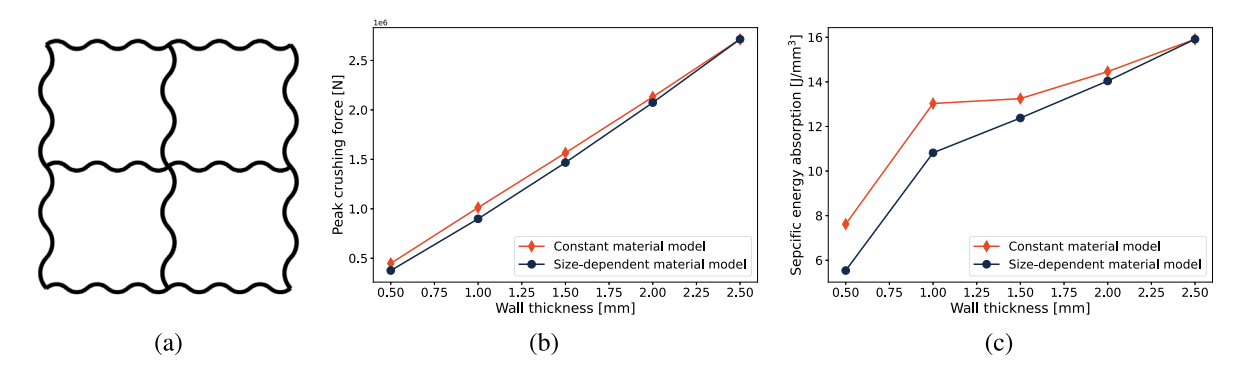


Fig. 12. Axial lattice compression at different lattice wall thicknesses: (a) Lattice cross section. (b) Comparison of PCF predicted by different models. (c) Comparison of SEA predicted by different models.

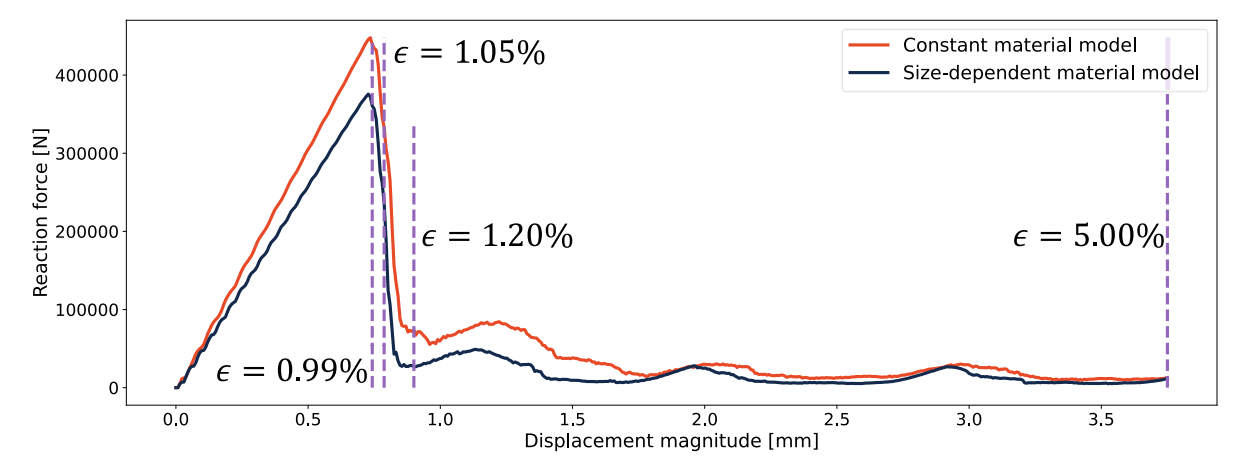


Fig. 13. The force-displacement curves predicted by two material models. Four points on the load path were marked for further discussion; they are 0.99%, 1.05%, 1.2%, and 5% axial compression strain, respectively. (For interpretation of the references to color in this figure legend, the reader is referred to the web version of this article.)

To compare the deformed shapes and fracture locations predicted by the two material models, the displacement magnitude and equivalent plastic strain contours at the four critical points are shown in Figs. 14 and 15.

Comparing the results in Fig. 12 and Table 3, it is evident that ignoring material size effects leads to over-prediction of PCF by an average of over 5% and SEA by an average of over 10%. In the most extreme case, when CM was used to model the lattice with 0.5 mm thickness, it overestimated the PCF by close to 20% and SEA by almost 40%. This overestimation of performance is undesirable in design areas

requiring a tight safety factor, such as the aerospace industry. Thus, material size dependence should be included in the constitutive model if a conservative estimate is needed. Inspecting the complete force—displacement curve, the deformed shape, and the fracture locations revealed that the lattice failed by local bucking at the center of its height. Noticeable out-of-plane buckling displacement is visible after the peak load at around 0.99% strain. Comparing the contours in the first column of Figs. 14 and 15, we see that SDM predicted larger buckling displacement magnitude and more widespread localized fracture, which contribute to the lower predicted PCF. At around nominal 1.05%

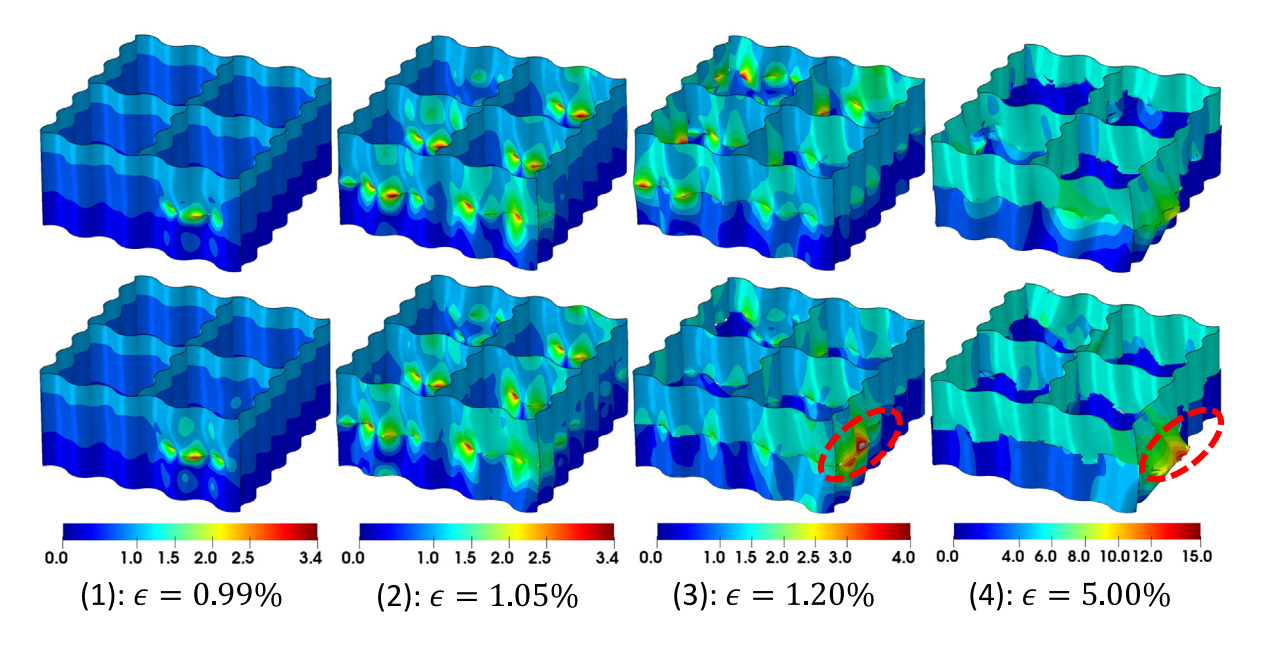


Fig. 14. The displacement magnitude predicted by two material models. Constant model predictions are on the top row, and size-dependent model predictions are on the bottom. Noticeable differences are circled in red. (For interpretation of the references to color in this figure legend, the reader is referred to the web version of this article.)

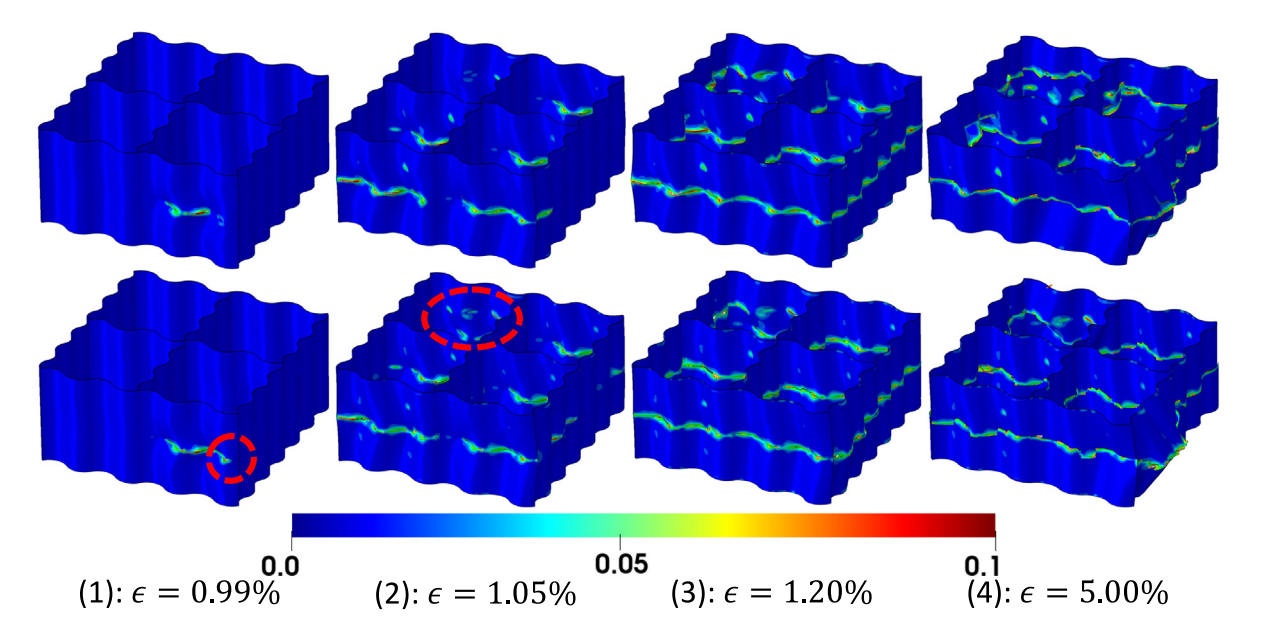


Fig. 15. The equivalent plastic strain predicted by two material models. Constant model predictions are on the top row, and size-dependent model predictions are on the bottom. Noticeable differences are circled in red. Fracture locations are shown with high equivalent plastic strain. (For interpretation of the references to color in this figure legend, the reader is referred to the web version of this article.)

compression strain, both material models predicted that the lattice went through a loss in strength caused by rapid localized buckling and fracture. Again, fracture is more widespread as predicted by SDM. At 1.2% strain, most of the structural strength was lost, and both models predicted similar fracture patterns. However, at 1.2% and 5% strain, SDM predicted a more pronounced localized buckling at the lower-right corner of the lattice, as highlighted in the last two columns of Fig. 14. These results indicate that ignoring material size effects can lead to different predicted deformed shapes and less widespread fracture at the initial stage of structural failure.

The lattices simulated in this example have constant thicknesses throughout the structure. In this case, it can be argued that a size-dependent material model is unnecessary, and it is easier to simply calibrate the material using the target wall thickness instead of a range

of thicknesses. However, this is only the case if the lattice wall thickness is already known. If the optimal lattice thickness for a given application is not known and is to be chosen from a range of acceptable thicknesses, a constant material model cannot fully capture the change in material response as wall thickness varies, and a size-dependent material model should be used.

3.4. Material size effects and topology optimization

The lattices in Section 3.3 have a uniform thickness distribution. However, in many real-world applications, the lattice wall thickness distribution may be nonuniform, such as functionally graded lattices generated from TO [34]. In this case, a material model calibrated over a single thickness cannot accurately capture the material behavior of a

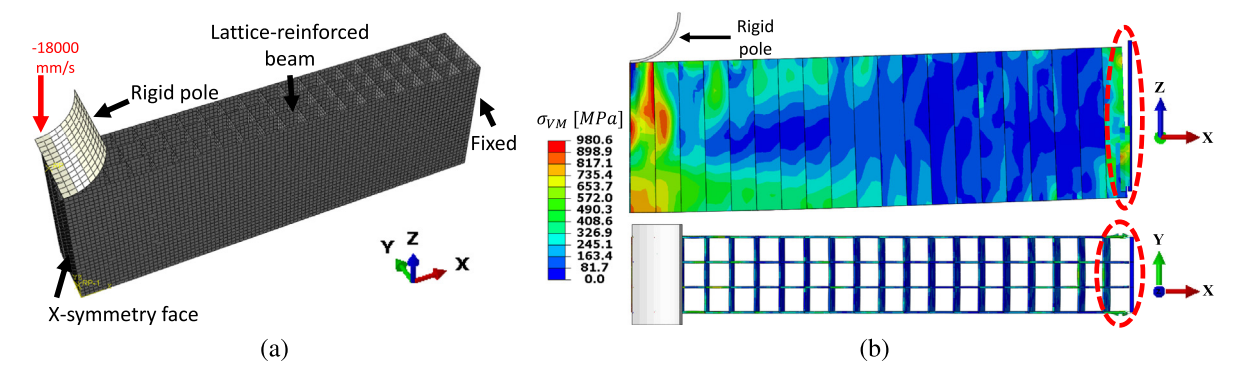


Fig. 16. FE model setup and deformation: (a) Mesh of the half beam model with applied boundary conditions. (b) The deformed initial design at the end of the simulation, colored by the von Mises stress. The top row shows the side view, while the bottom row shows the top view. Fracture occurred at the fixed end and is circled in red. (For interpretation of the references to color in this figure legend, the reader is referred to the web version of this article.)

multi-thickness design. The authors [35] recently developed a heuristic TO framework for thin-walled lattice structures to maximize SEA under dynamic loading by iteratively updating the wall thickness distribution. The mathematical statement of the optimization and design constraints are:

$$\max_{t} \frac{1}{V} \sum_{i=1}^{N} E^{i}$$
s.t. $V = \sum_{i=1}^{N} t^{i} L^{i} H^{i} = V^{*},$

$$t_{min} \leq t^{i} \leq t_{max}, \forall i = 1 \cdots N,$$

$$\|t^{i+1} - t^{i}\|_{\infty} \leq \Delta t_{max},$$
(13)

where E^i is the total energy absorbed by the ith lattice wall in the structure. t, L, and H denote the individual lattice wall's thickness, length, and height. V^* is the target volume of the lattice structure. t_{min} and t_{max} are user-defined thickness limits as a manufacturing constraint, and Δt_{max} is the maximum allowable thickness change per iteration. N is the number of lattice wall segments in a design. The design variables of this optimization are the thicknesses t of all lattice walls. Size-dependent material properties were not employed in the examples in [35]. In this example, we investigate how size effects influence the optimized design generated by TO.

Consider a lattice-reinforced rectangular beam with dimensions $400 \times 30 \times 60 \text{ mm}^3$ that is fixed at both ends. A rigid pole of 20 mm radius impacts the center of the beam at a downward velocity of 18000 mm/s for a displacement of 9 mm. Although the applied strain rate is high, we did not include strain-rate sensitivity effects in the material model and assumed that the material parameters are strainrate-independent. Symmetry in the YZ plane was exploited, so only half of the domain was modeled. The initial lattice design has a uniform wall thickness of 0.7 mm except for the non-designable walls at both ends where the fixed boundary condition is applied, whose thickness is 1.5 mm. The maximum and minimum allowable wall thicknesses are 2.5 and 0.5 mm, respectively. $\Delta t_{max} = 0.12$ mm allows relatively aggressive design change per iteration. The mesh and boundary conditions are shown in Fig. 16(a); a mesh size of 2 mm was used. The initial design's deformed shape and fracture locations are shown in Fig. 16(b). Forty TO iterations were performed to maximize the SEA of the beam while maintaining the same volume as the initial design. TO was performed independently with the constant and size-dependent material models.

The optimized designs occurred at design iterations 27 and 36 for CM and SDM, respectively. The signed thickness difference Δt is used to show differences in the designs, which is defined as:

$$\Delta t = t_{SDM} - t_{CM},\tag{14}$$

where t_{SDM} and t_{CM} denote the optimized thickness distribution arrays from SDM and CM, respectively. The two optimized designs and Δt are

 Table 4

 Energy absorption comparison for the two optimized designs.

	Total absorption	Elastic	Plastic	Damage
From constant model [J]	272.4	103.9	167.2	1.2
From size-dependent model [J]	334.3	168.7	165.3	0.3
Percent difference [%]	-18.5	-38.4	1.1	282.8

presented in Fig. 17(a). A histogram is shown in Fig. 17(b) to compare the distribution of lattice wall thicknesses in both optimized designs.

To provide a consistent comparison of the performance of the designs, SDM was used to simulate the response of the optimized designs and obtain a size-dependent estimate of their energy absorption. Fig. 18 depicts a bar chart showing the energy contributions, and Table 4 shows the numerical values. The final deformed shapes, plastic strain, and fracture distributions are shown in Fig. 19.

Comparing the optimized designs in Fig. 17(a), it is evident that material size effects influenced the optimized design generated from TO. Both structures share the common feature of a gradated horizontal wall thickness distribution, where the wall thickness is larger near the fixed end and the center where the rigid pole impacts. In addition, both designs removed vertical lattice wall members except at the fixed end and center. The crucial difference between the designs is that the one from CM distributed the structural volume approximately evenly over all four horizontal members. In comparison, SDM removed the top horizontal member (Row 1 in Fig. 17(a)) to distribute the same volume to only three horizontal members. Doing so effectively strengthened the remaining members. This behavior is expected, as SDM predicts that thinner lattice walls provide less energy absorption than their thicker counterparts, thus becoming a weak point in the design. Therefore, the optimizer moved material from the relatively stronger regions to the weaker regions, so the overall design is balanced. This trend is also observed in Fig. 17(b) as we see a rightward shift of average lattice wall thickness for the optimized design from SDM, and the design is dominated by lattice wall members with mid-range thicknesses (about 1.5 mm). Comparing the design performance in Fig. 18 and Table 4, it is revealed that the optimized design from SDM has about 19% higher SEA (both designs share identical total volume). Inspecting the detailed contributions to the total energy absorption, we see that the SDM design stores about 38% more energy through elastic deformation, while the irreversible plastic dissipation is almost identical (about 1%less) compared to the CM design. Noticeably, the SDM design also has less fracture at the end of the impact, although the magnitudes of the fracture dissipation are small compared to plasticity. For the fracture locations, from Fig. 16(b), we observed that for the uniformthickness design fractures were localized near the fixed end, and the lattice wall members connecting to the fixed end almost fractured completely. Both optimized designs did not suffer from fractures at the fixed wall, which is an improvement over the initial design. For the CM optimized design, through-height fractures exist around the center

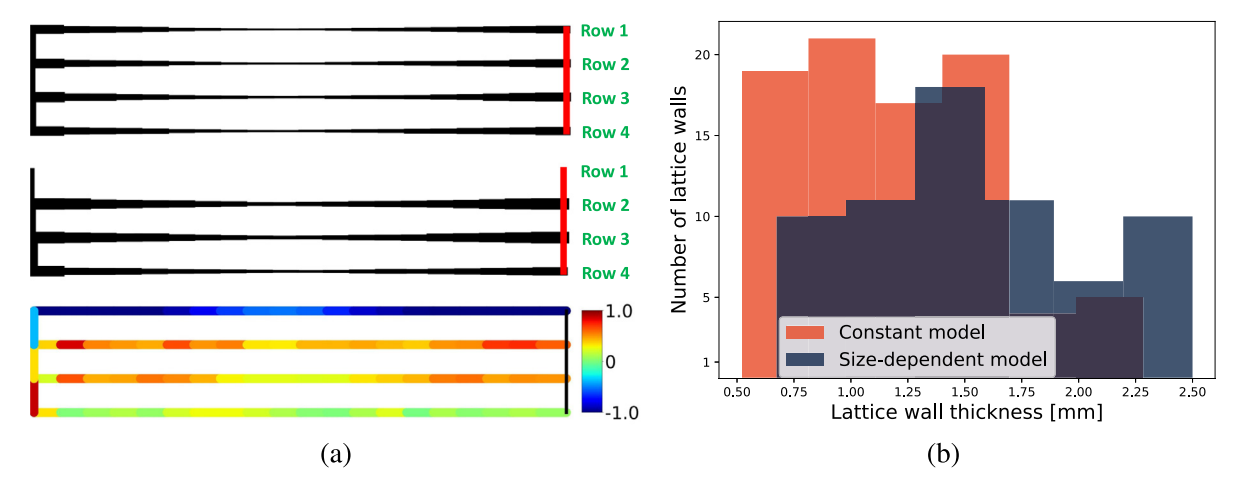


Fig. 17. TO-optimized designs comparison: (a) Optimized cross-section designs generated from two material models (top-down view). The line thickness is assigned based on lattice wall thickness; non-designable outer boundaries have a fixed thickness of 1.5 mm and are marked in red. The four rows of horizontal wall members are numbered for subsequent discussion. (b) A histogram comparing the thickness distributions. (For interpretation of the references to color in this figure legend, the reader is referred to the web version of this article.)

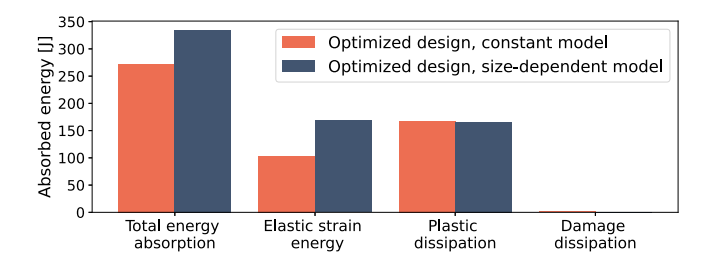


Fig. 18. Performance comparison between two optimized designs. All energy values reported here were calculated using the size-dependent material model.

of the structure (see the circled regions in Fig. 19(a)). For the SDM-optimized design, no through-height fractures were present. Compared to the initial design, the two optimized structures also extensively leveraged localized buckling as an energy absorption mechanism. These results indicate that the optimized design generated from SDM is more robust than one generated from CM; it has higher SEA though more effective elastic energy storage and is less susceptible to fracture.

In real-world applications, it is ubiquitous that a lattice design is to be generated to yield optimum performance under a set of anticipated loads. If a systematic optimization tool such as TO is used, the optimizer must traverse through a vast design space of lattice designs with different wall thicknesses before providing an optimized design. Therefore, it is impossible to calibrate the material model to a single wall thickness. In this case, having a size-dependent material model inherently provides more physical insights and information to the optimizer or designer when exploring different lattice designs or generating an optimized lattice design. We also emphasize that these arguments are valid regardless of whether the current material model is further validated by lattice-scale experiments or not. Therefore, from a lattice designer perspective, incorporating material size effects in the design process is vital to producing more robust designs.

4. Conclusions, limitations, and future work

This work presents an experimental and computational study on size effects in SLM Ti-6Al-4V samples. On the experimental side, flat tensile specimens of five different thicknesses were manufactured and tested under quasi-static tensile tests. The experimentally measured Young's modulus, yield stress, and elongation to failure decrease monotonically with specimen thickness, which agrees with previous experimental studies. Approximate analytical expressions of the size-dependence of material parameters were provided through curve fitting. The fitted

size-dependent material model was validated against experimental data with 1.5 mm specimen thickness. The simulated response well captures the mean behavior and falls within specimen-to-specimen variation.

On the computational side, two examples were presented to emphasize the importance of a size-dependent material model in evaluating and designing thin-walled lattices. In the first example, two material models were used to predict the PCF and SEA of a lattice design at different thicknesses. The results reveal that a material model that ignored size effects over-predicted the PCF and SEA by 19.2% and 37.6% in the most extreme case, respectively. In addition, the size-independent model under-predicted the buckling displacement magnitude and the extent of fracture during the first major structural failure. The results highlight that a size-independent material model calibrated at large specimen thickness provides overly optimistic design performance predictions and is undesirable in applications requiring a tight safety factor. In the second example, two material models were used in TO to improve the SEA of a lattice-reinforced beam. The size-dependent model produced a more balanced design with fewer lattice wall members; hence, the average thickness and strength increased. Comparison between the two optimized designs showed that the size-dependent design has higher SEA and no visible through-height fracture at the end of the loading, making it more robust than the one generated from the size-independent model. The results demonstrate that using a size-dependent material model in the lattice design process is highly necessary. Such a model provides more physical information on the material behavior as the optimizer traverses through different thicknesses and can produce a more robust optimized design.

The limitations of the present work are as follows. All the characterization tests were performed under quasi-static conditions at a single strain rate. Hence, the current size-dependent material model does not account for the effects of strain rate on material behavior. In all the numerical examples, this material model was applied even when the applied strain rate was high, and we operated under the assumption that the strain rate effects would influence the constant and size-dependent material models in the same way. Secondly, we could not extract size-dependent fracture energy from the experiments due to the low camera frame rate. The fracture energy, like the equivalent plastic strain at damage initiation, is a crucial parameter defining material failure behavior and can be size-dependent. Therefore, we assumed constant failure energy in this work and calibrated the damage initiation strain to match the global failure behavior. Lastly, the current material model was only validated with tensile test data and was not compared with lattice-scale experimental results. However, we remark that the arguments we made about the importance of a size-dependent

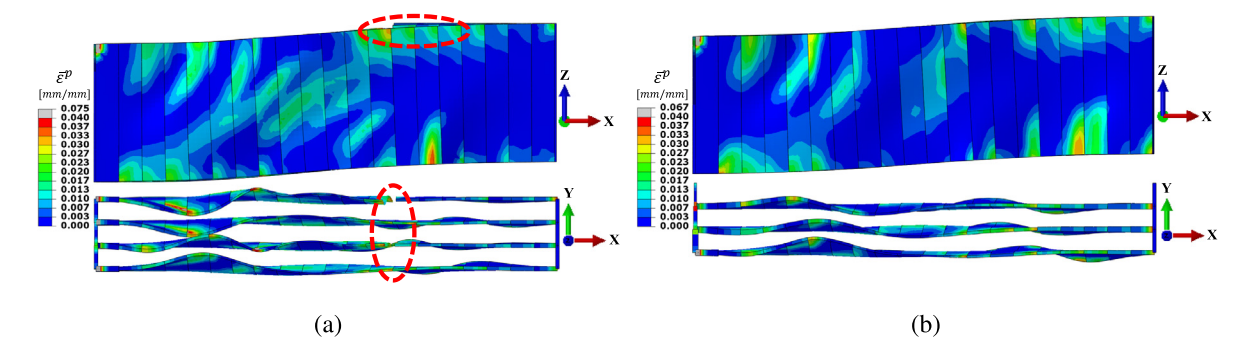


Fig. 19. Comparison of plastic strain and fracture distributions: (a) Optimized design generated from constant model. (b) Optimized design generated from the size-dependent model. The top row shows the side view, while the bottom row shows the top view. Fracture locations are circled in red. (For interpretation of the references to color in this figure legend, the reader is referred to the web version of this article.)

material model in the lattice design process remain valid regardless of whether the current model is further validated by lattice compression experiments.

In future work, we aim to perform additional experiments to address the limitations of this work: (1) to perform tensile tests at various strain rates, especially covering the high-strain-rate regime, to characterize how strain rate affects the size-dependent material behavior; (2) conduct lattice compression experiments and compare the results with the predicted response from the size-dependent material model to validate its application on full lattices; and (3) perform additional experiments to determine the failure strain under buckling, as local buckling commonly occurs in compression of thin-walled lattices.

Replication of results

The data and source code that support the findings of this study can be made available upon reasonable request to the corresponding author.

CRediT authorship contribution statement

Junyan He: Writing – original draft, Software, Methodology, Investigation, Formal analysis, Data curation, Conceptualization. Shashank Kushwaha: Writing – original draft, Methodology, Investigation, Formal analysis. Mahmoud A. Mahrous: Writing – original draft, Methodology, Investigation, Formal analysis. Diab Abueidda: Writing – review & editing, Supervision. Eric Faierson: Writing – review & editing, Supervision, Resources. Iwona Jasiuk: Writing – review & editing, Supervision, Resources, Funding acquisition.

Declaration of competing interest

The authors declare that they have no known competing financial interests or personal relationships that could have appeared to influence the work reported in this paper.

Data availability

Data will be made available on request.

Acknowledgments

We (I. J.) acknowledge the support of the Army Research Office, United States contract (No. W 911NF-18-2-0067) and the National Science Foundation, United States grant (MOMS-1926353). This research is also a part of the Delta research computing project, which is supported by the National Science Foundation, United States (award OCI 2005572) and the State of Illinois. We acknowledge the valuable discussion we had with Dr. Jeffrey Lloyd from the U.S. Army Research Laboratory. We also acknowledge the help of Drs. David Ehrhardt and Peter Kurath from the Advanced Materials Testing and Evaluation Laboratory (AMTEL) at the University of Illinois at Urbana-Champaign in testing the specimens.

References

- Tomas Kellner, An epiphany of disruption: GE additive chief explains how 3D printing will upend manufacturing, GE Rep. 13 (2017).
- [2] Syed AM Tofail, Elias P Koumoulos, Amit Bandyopadhyay, Susmita Bose, Lisa O'Donoghue, Costas Charitidis, Additive manufacturing: scientific and technological challenges, market uptake and opportunities, Mater. Today 21 (1) (2018) 22–37
- [3] J.A. Harris, R.E. Winter, G.J. McShane, Impact response of additively manufactured metallic hybrid lattice materials, Int. J. Impact Eng. 104 (2017) 177–191
- [4] Nattapon Chantarapanich, Apinya Laohaprapanon, Sirikul Wisutmethangoon, Pongnarin Jiamwatthanachai, Prasert Chalermkarnnon, Sedthawatt Sucharitpwatskul, Puttisak Puttawibul, Kriskrai Sitthiseripratip, Fabrication of threedimensional honeycomb structure for aeronautical applications using selective laser melting: a preliminary investigation, Rapid Prototyp. J. 20 (6) (2014) 551–558.
- [5] Judyta Sienkiewicz, Paweł Płatek, Fengchun Jiang, Xiaojing Sun, Alexis Rusinek, Investigations on the mechanical response of gradient lattice structures manufactured via SLM, Metals 10 (2) (2020) 213.
- [6] Eric Yang, Martin Leary, Bill Lozanovski, David Downing, Maciej Mazur, Avik Sarker, AmirMahyar Khorasani, Alistair Jones, Tobias Maconachie, Stuart Bateman, et al., Effect of geometry on the mechanical properties of Ti-6Al-4V gyroid structures fabricated via SLM: A numerical study, Mater. Des. 184 (2019) 108165
- [7] Shuai Ma, Qian Tang, Qixiang Feng, Jun Song, Xiaoxiao Han, Fuyu Guo, Mechanical behaviours and mass transport properties of bone-mimicking scaffolds consisted of gyroid structures manufactured using selective laser melting, J. Mech. Behav. Biomed. Mater. 93 (2019) 158–169.
- [8] Xiaofei Cao, Dengbao Xiao, Ying Li, Weibin Wen, Tian Zhao, Zihao Chen, Yongbo Jiang, Daining Fang, Dynamic compressive behavior of a modified additively manufactured rhombic dodecahedron 316L stainless steel lattice structure, Thin-Walled Struct. 148 (2020) 106586.
- [9] Dexing Qi, Huabin Yu, Ming Liu, Han Huang, Shucai Xu, Yong Xia, Guian Qian, Wenwang Wu, Mechanical behaviors of SLM additive manufactured octet-truss and truncated-octahedron lattice structures with uniform and taper beams, Int. J. Mech. Sci. 163 (2019) 105091.
- [10] AmirMahyar Khorasani, Ian Gibson, Umar Shafique Awan, Alireza Ghaderi, The effect of SLM process parameters on density, hardness, tensile strength and surface quality of Ti-6Al-4V, Addit. Manuf. 25 (2019) 176–186.
- [11] Luke N Carter, Christopher Martin, Philip J Withers, Moataz M Attallah, The influence of the laser scan strategy on grain structure and cracking behaviour in SLM powder-bed fabricated nickel superalloy, J. Alloys Compd. 615 (2014) 338–347.
- [12] John J. Lewandowski, Mohsen Seifi, Metal additive manufacturing: A review of mechanical properties, Annu. Rev. Mater. Res. 46 (2016) 151–186.
- [13] Rakish Shrestha, Jutima Simsiriwong, Nima Shamsaei, Fatigue behavior of additive manufactured 316L stainless steel parts: Effects of layer orientation and surface roughness. Addit. Manuf. 28 (2019) 23–38.
- [14] Wei Xu, M Brandt, S Sun, J Elambasseril, Q Liu, K Latham, K Xia, M Qian, Additive manufacturing of strong and ductile Ti-6Al-4V by selective laser melting via in situ martensite decomposition, Acta Mater. 85 (2015) 74-84.
- [15] Marco Simonelli, Yau Yau Tse, Christopher Tuck, Effect of the build orientation on the mechanical properties and fracture modes of SLM Ti-6Al-4V, Mater. Sci. Eng. A 616 (2014) 1–11.
- [16] D Barba, C Alabort, YT Tang, MJ Viscasillas, RC Reed, E Alabort, On the size and orientation effect in additive manufactured Ti-6Al-4V, Mater. Des. 186 (2020) 108235.
- [17] Chinmay Phutela, Nesma T Aboulkhair, Christopher J Tuck, Ian Ashcroft, The effects of feature sizes in selectively laser melted Ti-6Al-4V parts on the validity of optimised process parameters, Materials 13 (1) (2019) 117.

- [18] Ashley M Roach, Benjamin C White, Anthony Garland, Bradley H Jared, Jay D Carroll, Brad L Boyce, Size-dependent stochastic tensile properties in additively manufactured 316l stainless steel, Addit. Manuf. 32 (2020) 101090.
- [19] Ahmad Alghamdi, David Downing, Rance Tino, Abduladheem Almalki, Tobias Maconachie, Bill Lozanovski, Milan Brandt, Ma Qian, Martin Leary, Buckling phenomena in AM lattice strut elements: A design tool applied to Ti-6Al-4V LB-PBF, Mater. Des. 208 (2021) 109892.
- [20] Zhichao Dong, Xiaoyu Zhang, Wenhua Shi, Hao Zhou, Hongshuai Lei, Jun Liang, Study of size effect on microstructure and mechanical properties of AlSi10Mg samples made by selective laser melting, Materials 11 (12) (2018) 2463.
- [21] Morton E. Gurtin, Lallit Anand, Thermodynamics applied to gradient theories involving the accumulated plastic strain: the theories of Aifantis and Fleck and Hutchinson and their generalization, J. Mech. Phys. Solids 57 (3) (2009) 405–421.
- [22] John Hutchinson, Norman Fleck, Strain gradient plasticity, Adv. Appl. Mech 33 (1997) 295–361.
- [23] H. Gao, Y. Huang, W.D. Nix, J. Hutchinson, Mechanism-based strain gradient plasticity—I. Theory. J. Mech. Phys. Solids 47 (6) (1999) 1239–1263.
- [24] Bill Lozanovski, Martin Leary, Phuong Tran, Darpan Shidid, Ma Qian, Peter Choong, Milan Brandt, Computational modelling of strut defects in SLM manufactured lattice structures, Mater. Des. 171 (2019) 107671.
- [25] Mohammad Taufik, Prashant K. Jain, Role of build orientation in layered manufacturing: a review, Int. J. Manuf. Technol. Manag. 27 (1-3) (2013) 47-73
- [26] Ruben Wauthle, Bey Vrancken, Britt Beynaerts, Karl Jorissen, Jan Schrooten, Jean-Pierre Kruth, Jan Van Humbeeck, Effects of build orientation and heat treatment on the microstructure and mechanical properties of selective laser melted Ti6Al4V lattice structures, Addit. Manuf. 5 (2015) 77–84.
- [27] Xuemei Wang, Jun Shi, Validation of Johnson-Cook plasticity and damage model using impact experiment, Int. J. Impact Eng. 60 (2013) 67–75.

- [28] J.-H. Kim, A. Serpantié, F. Barlat, F. Pierron, M-G Lee, Characterization of the post-necking strain hardening behavior using the virtual fields method, Int. J. Solids Struct. 50 (24) (2013) 3829–3842.
- [29] SIMULIA, Abaqus, 2020.
- [30] Arne Hillerborg, Mats Modéer, P.-E. Petersson, Analysis of crack formation and crack growth in concrete by means of fracture mechanics and finite elements, Cem. Concr. Res. 6 (6) (1976) 773–781.
- [31] Pauli Virtanen, Ralf Gommers, Travis E. Oliphant, Matt Haberland, Tyler Reddy, David Cournapeau, Evgeni Burovski, Pearu Peterson, Warren Weckesser, Jonathan Bright, Stéfan J. van der Walt, Matthew Brett, Joshua Wilson, K. Jarrod Millman, Nikolay Mayorov, Andrew R.J. Nelson, Eric Jones, Robert Kern, Eric Larson, C J Carey, İlhan Polat, Yu Feng, Eric W. Moore, Jake VanderPlas, Denis Laxalde, Josef Perktold, Robert Cimrman, Ian Henriksen, E.A. Quintero, Charles R. Harris, Anne M. Archibald, Antônio H. Ribeiro, Fabian Pedregosa, Paul van Mulbregt, SciPy 1.0 Contributors, SciPy 1.0: Fundamental Algorithms for Scientific Computing in Python, Nature Methods 17 (2020) 261–272, http://dx.doi.org/10.1038/s41592-019-0686-2.
- [32] F. Tarlochan, A.M.S. Hamouda, E. Mahdi, B.B. Sahari, Composite sandwich structures for crashworthiness applications, Proc. Inst. Mech. Eng. L J. Mater. Des. Appl. 221 (2) (2007) 121–130.
- [33] Junyan He, Shashank Kushwaha, Diab Abueidda, Iwona Jasiuk, Exploring the structure-property relations of thin-walled, 2D extruded lattices using neural networks, Comput. Struct. 277 (2023) 106940.
- [34] Ajit Panesar, Meisam Abdi, Duncan Hickman, Ian Ashcroft, Strategies for functionally graded lattice structures derived using topology optimisation for additive manufacturing, Addit. Manuf. 19 (2018) 81–94.
- [35] Junyan He, Shashank Kushwaha, Diab Abueidda, Iwona Jasiuk, LatticeOPT: a heuristic topology optimization framework for thin-walled, 2D extruded lattices, Struct. Multidiscip. Optim. 65 (11) (2022) 308, http://dx.doi.org/10.1007/ s00158-022-03397-5